Journal of Materials Chemistry A

Accepted Manuscript

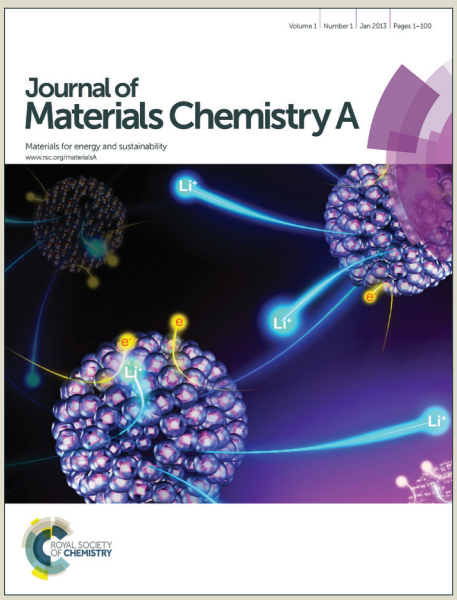

ROYAL SOCIETY OF CHEMISTRY

www.rsc.org/materialsA

Cite this: DOI: 10.1039/c0xx00000x

www.rsc.org/xxxxxx

ARTICLE TYPE

A simple, room temperature, solid-state synthesis route for metal oxide nanostructures †

Supriya A. Patil,[a] Dipak V. Shinde, [a] Do Young Ahn,[a] Dilip V. Patil,[a] Kailas K.Tehare,[b] Vijaykumar V. Jadhav,[b] Joong K. Lee,[c] Rajaram S. Mane,[b] Nabeen K. Shrestha,[a] Sung-Hwan Han,[a]*

Received (in XXX, XXX) Xth XXXXXXXXX 20XX, Accepted Xth XXXXXXXXX 20XX
DOI: 10.1039/b000000x

In this work, we demonstrate an extremely simple but highly effective strategy for the synthesis of various functional metal oxides (MOs) such as ZnO, In_2O_3, Bi_2O_3, and SnO_2 nanoparticles with various distinct shapes at room temperature *via* a solid-state reaction method. The method involves only mixing and stirring the corresponding metal salt and NaOH together in solid phase, which yields highly crystalline metal oxides within 5 - 10 min of reaction time. The obtained paste can be directly doctor-bladed onto variety of substrates for photoelectrochemical applications. The crystal structure and surface composition of the MOs are obtained by X-ray diffraction patterns, energy dispersive analysis and X-ray photoelectron spectroscopy, respectively. Surface morphology is confirmed from the scanning electron microscopy surface photo-images. Surface area and pore size distribution is studied by N_2 adsorption method. As a proof-of-concept demonstration for the application, ZnO nanoplate structures are envisaged in DSSCs as photoanode, which enables us to obtain excellent photovoltaic properties with power conversion efficiency of 5%. The proposed method does not require sophisticated instrumental setup or harsh conditions, and the method is easily scalable. Hence, it can be applied for the cost-effective and large-scale production of MO nanoparticles with high crystallinity.

Introduction

Growth of MO nanoparticles has attracted much attention in recent years because of their application in variety of optoelectronic devices.[1] Basically, MOs are ionic compounds that are made up of positive metallic and negative oxygen ions. The electrostatic interactions between the positive metallic and negative oxygen ions result in solid ionic bonds. Additionally, the *s*-shells of MOs are completely filled, so that most of them have excellent thermal and chemical stabilities.[2,3] However, their *d*-shells perhaps are not completely filled, producing a variety of unique properties that make them potentially of great use in electronic devices. These unique properties include wide band gaps,[4,5] high dielectric constants, reactive electronic transitions,[6,7] and good electrical, optical,[8,9] electrochromic characteristics,[10,11] and superconductivity.[12,13] Therefore, MOs are considered as the most fascinating functional materials and have been widely exploited in various technological applications.[14-17] With the growing emphasis of the current science and technology on nanomaterials, and due to their unique and novel properties, considerable efforts are being made in the past decade to synthesize various metal oxides such as TiO_2, ZnO, In_2O_3, Bi_2O_3, SnO_2 and SnO *etc*. in the form of different phases and shapes using a variety of chemical and physical synthesis techniques. Such metal oxide nanostructures have demonstrated a promising application in various fields such as electrochromism, supercapacitor, field emission, LED, DSSCS, etc.[18-24] Depending on the use of a particular process, precursor, capping agent, complex agent, temperature, pressure *etc*., are needed to be optimized. In the perspective of different applications such as photovoltaics, catalysis, electro-optics *etc*., controlled synthesis of MO growth is well studied.[25] However, different MOs show stability-dependent crystal growth which make the proposition of developing specific shaped morphology.[26] Considering the potential of MOs, dye sensitized solar cells (DSSCs) could grip the balance in the future energy production and take up a considerable market share in energy supply. To serve, MOs nanostructured photoanodes constructed by facile, low-cost and scalable methods are highly desirable.[27-30] There are several methods for fabrication of MO nanostructures, such as thermal evaporation, dc-plasma reaction, chemical vapour deposition, molecular beam epitaxy, sputtering and solution-derived synthesis, and so on.[31-35]

Above mentioned methods, however, require particular experimental conditions, additives, complicated instrumental setup, making it difficult to scale-up the production. The development of cost-effective and environment friendly methods, suitable for the large-scale synthesis of MOs nano and microstructures is therefore of a great demand. In the same line, we report here a solid-state synthesis route as an inexpensive, simple, and environmentally friendly approach for preparing

MOs *viz*. ZnO, In_2O_3, Bi_2O_3 and SnO_2. At room temperature, via a solid-state reaction between two commonly available low cost reactants - i.e., reacting NaOH with metal precursors such as $Zn(NO_3)_2$, $InCl_3$, $BiCl_3$ and $SnCl_4$, nanoparticles of ZnO, In_2O_3, Bi_2O_3 and SnO_2, respectively could be synthesized rapidly within 5 - 10 min (Scheme 1and Figure 1). In addition, the as-formed materials exhibited high crystallinity without any thermal treatment.[36-40] Furthermore, as a proof-of-concept demonstration for the application of such MOs nanostructures, we investigated the ZnO nanoplate-based photoanode from these four MOs for DSSC application, which showed excellent photovoltaic performances. To more thoroughly understand the properties of these ZnO nanoplate-based photoanodes and synthesis mechanism, we systematically carried out structural, optical, and electrochemical measurements.

Experimental

Chemicals

All reagents used in the present work were of analytical grade, and used without further purification. Zinc nitrate ($Zn(NO_3)_2.6H_2O$, 98 %, Deaejung Chemicals, S. Korea), indium chloride ($InCl_3$, 99.999 %, Alfa Aesar), bismuth chloride ($BiCl_3$, 98 %, Alfa Aesar), tin chloride ($SnCl_4$, 98 %, Alfa Aesar) and sodium hydroxide (NaOH, 97 %, Kanto Chemicals, Japan) were used as received. Triply-distilled water was used throughout the experiment. N719 dye is obtained from *Solaronix* SA, Switzerland.

Synthesis

MOs nanostructures were synthesized by using solid-state reaction between two commonly available and low cost reactants, i.e. $Zn(NO_3)_2$, $InCl_3$, $BiCl_3$, $SnCl_2$ and NaOH. In a typical solid-state synthesis of MOs nanostructures, 10 g powder of each metal precursor and 5 g NaOH (2:1 w/w) were mixed together into a glass vial without adding any solvent, and the mixture was stirred using a magnetic stir bar for 5 - 10 min. After completion of the reaction, a thick slurry paste was obtained. The products were washed by dispersing them into water and separated using centrifugation. The washing step was repeated three times. Finally, without drying, the obtained MOs nanostructures were dispersed again into 15 ml deionised water and 5 ml ethanol (3:1 v/v) to prepare a homogeneous paste for the fabrication of thin films using doctor blade technique.

We choose ZnO photoanode for further study because of its excellent properties as anodes in DSSCs.[41-44]

DSSCs fabrication

Fluorine doped tin oxide (FTO) glass substrates used for doctor blading were first cleaned in detergent water, acetone and isopropyl alcohol for 10 min each using an ultrasonic bath. Then, these substrates were dried in a stream of argon and stored for further use. The doctor-blade technique was used to fabricate ZnO photoanodes without using any binder. After drying in air, the photoanode films were thermally treated at a fixd 150 $^{\circ}$C, 250 $^{\circ}$C, 350 $^{\circ}$C and 450 $^{\circ}$C temperatures for 60 min, and then sensitized with 0.5 mM N719 prepared in absolute ethanol: acetonitrile (1:1 v/v) solution for 60 min.[45]

Characterizations

The crystal structures and phases of metal oxides were confirmed using X-ray diffraction patterns (XRD) obtained on an X-ray diffractometer (Rigaku D/MAX 2500 V, Cu-Ka, λ =0.15418 nm). The chemical composition of the MOs is determined using an energy dispersive X-ray analyser (EDX, EM912) coupled to a scanning electron microscope (SEM, Hitachi S-4200). Transmission electron microscopy (TEM) measurements were performed on a JEOL-2100F transmission electron microscope with an acceleration voltage of 100 kV. The samples for TEM analysis were prepared by dropping about 20 µl of diluted solution of nanostructures in ethanol onto carbon-coated copper grids and slowly drying in air. The morphology of electrodes was monitored using the SEM (Hitachi S-4200). In order to measure the solar-to-electric power conversion efficiency, electrodes were incorporated into thin layer sandwich-type cells with a Pt coated FTO as the counter electrode using a spacer film (50 mm thick polyimide film). Cell performance was measured by irradiation of 100 mW cm^2 white light (1 Sun, 1.5 AM) using a solar simulator (PEC-L01, Peccell). Current density was measured using a Keithley 2400 source meter by defining a definite area of 0.25 cm^2 of the photoanode. Electrochemical impedance spectroscopy (EIS) spectra were obtained using an Ivium CompactStat impedance analyzer in the range of 0.01 Hz to 1.5 MHz. All spectra were recorded at open circuit conditions under 1 Sun illumination. The data was fitted using Z-view software. The incident photon-to-current conversion efficiency (IPCE) was recorded without bias under illumination with respect to a calibrated Melles-Friot silicon diode and measured by changing the excitation wavelength (photon counting spectrometer, ISS Inc. and Keithley 2400). The *Brunauer-Emmett-Teller* (BET) surface areas of the MOs were calculated from N_2 adsorption isotherms, obtained using an ASAP-2010 instrument (Micromeritics) at 77 K. Amount of dye loading was estimated colorimetrically by desorbing the adsorbed dye in 0.1M NaOH solution made in ethanol and water (1:1 ratio) mixture.

Results and discussion

Reactions leading to the formation of MOs by the reaction of metal salts and sodium hydroxide can be given as below; [46]

$$Zn(NO_3)_2 + 2NaOH \longrightarrow Zn(OH)_2 + 2Na(NO_3) \quad (1)$$
$$Zn(OH)_2 \longrightarrow ZnO + H_2O \quad (2)$$
$$InCl_3 + 3NaOH \longrightarrow In(OH)_3 + 3\,NaCl \quad (3)$$
$$2In(OH)_3 \longrightarrow 2In_2O_3 + 3H_2O \quad (4)$$
$$BiCl_3 + 3NaOH \longrightarrow Bi(OH)_3 + 3\,NaCl \quad (5)$$
$$2Bi(OH)_3 \longrightarrow 2Bi_2O_3 + 3H_2O \quad (6)$$
$$SnCl_4 + 4NaOH \longrightarrow Sn(OH)_4 + 4\,NaCl \quad (7)$$
$$Sn(OH)_4 \longrightarrow SnO_2 + 2H_2O \quad (8)$$

Here, the water of crystallization and little moisture absorbed by the reactants might have enough to initialize ionization of a very small amount of the reaction precursors. When the ions from the reactants come to in contact, the precipitation reaction takes place immediately with the evolution of heat. This heat assists further to fuse the reactants and proceed the reaction ahead. Thus, sodium hydroxide reacts first with metal salt, yielding the

corresponding metal hydroxide, which further decomposes to produce metal oxide nanostructures. After washing as described in the experimental section, the reaction products were highly pure in the sense that the impurities were below the detectable range of the EDX and XPS analysis. SEM images and XRD patterns of the doctor bladed MO films are shown in Figure 2 and Figure 3, respectively. EDX spectra for In_2O_3, Bi_2O_3 and SnO_2 are shown in supporting information (Figure S1).Some higher oxygen content than the stoichiometric ratio can be observed, which could be due to the oxygen signals coming from the glass substrates that were used to deposit the doctor blade oxide films. However, the XRD patterns strongly support the formation of the MOs as revealed by the above reactions (1) – (8). The elegancy of this method lies in the fact that it forms highly crystalline metal oxide nanostructures at room temperature without any thermal treatment. In fact, the reactions of metal salts with NaOH are exothermic and this locally produced heat may be helping to crystallize the products. As a proof-of-concept demonstration for the application of MOs synthesized by the current method, ZnO nanostructures were investigated as photoanode materials in DSSCs, which is discussed in detail in the following paragraphs. Form the above reactions (1) and (2), ZnO in the form of fine nanoplate like morphology was obtained, which can be confirmed from SEM images shown in Figure 4a and b. Some of these nanoplates look like fused to each other. We believe that the fused nanoplates are favourable for charge collection and transportation due to their better connectivity. Figure 4b shows low magnified SEM image after annealing at 250 °C, which indicates highly porous and sponge like nature of the film. Traditionally, spongy and porous films, which are highly desirable for photoanode, are generally fabricated using pore forming agents. After synthesis, the products are required to anneal at higher temperature to remove the pore forming agents.[47] In contrast, the current method inherently produces ZnO porous structure composed of interconnected nanoplates, without using any external pore forming organic/inorganic agents at room temperature. This property is useful in DSSCs, where porous structure with good interconnectivity is necessary for high dye loading and accelerated charge transport. From the TEM image shown in Figure 4c, it can be seen that the ZnO nanocrystals with average diameter of 50 ~ 60 nm are uniformly fused in a nanoplate shaped fashion. The SAED pattern shown in Figure 4d indicates that the ZnO nanoplates are crystalline and a hexagonal wurtzite structure. This result is in line with the XRD pattern shown in Figure 5a.[48] The XRD pattern matches well with the JSPDS file no.36-1451 with crystalline nature.[49] Inset of Figure 4c shows high resolution TEM image of a single ZnO particle, which reveals a *d* spacing of 0.52 nm corresponding to 0001 plane of ZnO. Further chemical composition of the nanoplates was investigated using an XPS. Figures 5b, 5c and 5d show the XPS survey spectrum, and Zn 2p and O 1s core level spectra, respectively. Peaks at 1022.45 and 1045.47 eV of the Figure 5c correspond to the doublet of Zn 2p 3/2 and 2p 1/2, respectively, as has been reported previously for ZnO.[50]

The above ZnO nanostructures were employed as photoanode in DSSCs using the doctor-blade method. For this, ZnO thin films were fabricated by doctor blading the ZnO paste on a FTO glass substrate. Initially, we prepared two cells:- one was as-synthesized and another was thermally treated at 350 °C. The photoanode annealed at 350 °C exhibited an open circuit voltage (V_{oc}) of ~0.62 V, current density (J_{sc}) of ~11.42 mA cm^{-2}, fill factor (*ff*) of ~0.64, and power conversion efficiency (η) of ~4.5%. Inspired from this result, we further treated the ZnO photoanode at various temperatures (150 °C, 250 °C, 350 °C and 450 °C), keeping all other conditions such as dye loading and annealing time constant, expecting a higher η**.** Figure 6a shows the current-voltage (*J-V*) curves of the as-synthesized and the annealed photoanodes. It is clear from Figure 6a and Table 1 that the photoanode annealed at 250 °C shows the maximum power conversion efficiency of 5%. Initially, as the annealing temperature increases, there is increase in η up to 250 °C. After that, it decreases to 4.5 and finally to 4.1% for the 450 °C annealed sample. This can be explained on the basis of the fact that, bulk defects and surface states that play an important role in charge transfer and recombination processes in DSSCs, are strongly dependant on annealing temperature. The as-synthesized and the annealed smaples at lower temperature have high density of surface states, which in turn causes severe recombination of photogenerated electrons. Also, as there are plenty of grain boundaries exist in samples annealed at lower temperature, bulk trap states are higher, which pose severe recombination problems. It is clear from the cross-sectional SEM image in Figure 7a that the ZnO photoanodes are spongy and highly porous in nature. Furthermore, to investigate the effect of annealing temperature on the DSSCs photoanode, we characterized the surface area and the pore-size distribution of the five porous ZnO films annealed at different temperatures. Porosity strongly determines important physical properties of materials such as durability, mechanical strength, permeability, adsorption properties, etc. Pores are classified according to three main groups depending on the access size. For example, pores smaller than 2 nm in diameter are called as micropores, pores between 2 and 50 nm in diameter are called as mesopores, and pores larger than 50 nm in diameter are called as macrospores. The N_2 adsorption-desorption isotherms of the as-synthesized and the photoanodes treated at different temperatures are shown in Figure 7b (annealed at 250 °C) and Figure S2a (as-synthesized and treated at 150, 350 and 450 °C). Pore size distributions of these five photoanode films are shown in Figure S2b. Based on the above classification, the isotherm obtained for the ZnO photoanodes can be classified as type III, indicating that the pores in the photoanode are macroporous. There is a reduction in surface area from 23.55 to 6.42 $m^2 g^{-1}$ when annealing temperature was increased from 150 to 450 °C. Reduction in surface area could be due to the increase in crystallinity after annealing process. Porosities of the as-synthesized and the annealed ZnO electrodes are found to be ~33.37%, ~55.29 % (150 °C), ~64.29% (250 °C), ~59.24% (350 °C) and ~57.58% (450 °C). The pore volumes of these samples are also found to be in the more or less similar trend with the highest volume of 0.22 cm^3g^{-1} for the sample annealed at 250 °C. The porosity of the above ZnO products obtained after annealing increased initially and then decreased with the increase in annealing temperature. The initial increase in porosity may be due to the removal/evaporation of impurities present in ZnO matrix, whereas, further decrease in porosity can be assigned to an increase in crystallite size, which might have covered available

space/voids with an increase in annealing temperature. This merging and connectivity of small nanoplates at an elevated temperature is necessary for the electron transport in porous film.[51] The degree of dye loading is one of the key factor for better power conversion efficiency of a DSSC, which strongly depends on the porosity of photoanodes. Table 1 shows the amount of dye loading on ZnO photoanodes annealed at different temperatures.[52-54] The dye loading amount for the photoanode annealed at 250 °C is 2.91×10^{-7} molcm^{-2}, which is slightly higher than in other photoanodes - for example; 2.33×10^{-7} molcm^{-2} 2.72×10^{-7} molcm^{-2}, 2.86×10^{-7} molcm^{-2}, 2.84×10^{-7} molcm^{-2} for the as-synthesized and the samples annealed at 150 °C, 350 °C and450 °C, respectively. Thus, the above data suggests that the photoanode (for instance the sample annealed at 250 °C) with high porosity (64.29%), large pore volume (0.22 cm^{3}g^{-1}), and high dye-loading amount (2.91×10^{-7} molcm^{-2}) exhibits better photovoltaic performance.

To investigate the charge transport in the photoelectrode and charge recombination at the photoelectrode/electrolyte interface, electrochemical impedance spectroscopy (EIS) measurements were carried out for all ZnO photoanodes under illumination (100 mW.cm^{-2}, AM 1.5). The Nyquist plots are shown in Figure 6b. Figure 6c shows the zoom view of Nyquist plots at high frequency region. The charge transfer resistance estimated by fitting the experimental data are shown in Table 1. Generally, three typical frequency peaks are observed in EIS spectra of DSSCs. The ohmic series resistance R_s corresponds to the electrolyte and electronic contact in the device. The small semicircle at high frequency (>kHz) results from the charge transfer resistance at the Pt/electrolyte solution interface (R_{ct1}). The large semicircle at low frequency (10-100Hz) corresponds to the resistance at ZnO photoanode-dye/electrolyte interface (R_{ct2}). In addition, the semicircle at lowest frequency range is related to the diffusion process of I^-/I_3^- in the electrolyte (R_{diff}). The fitted Rs, Rct_1 and Rct_2 values for the ZnO photoanode treated at different temperatures are shown in Table 1. In the impedance spectra of ZnO photoanode, the values of R_{ct1} are nearly same, being about 2.8~3.7 Ω range, since the factors affecting this value are identical in all the fabricated devices (i.e. electrolyte and pt counter electrode). R_{ct2} is the main component determining the final energy conversion efficiency. It depends on the charge transport through the photoanode. It is clear from the Table 1 that Rct_2 value varies greatly and is strongly dependant on annealing temperature. This is obvious, since the crystallinity and interconnectivity play important role in generation and transport of photogenerated electrons. The device with the highest efficiency shows the lowest value of R_{ct2}, which means that the photogenerated electrons can easily flow through the photoanode with much less chances of recombination.[51]Bode phase plots of the DSSCs are shown in Figure S4. According to EIS model developed by litrature,[55] the electron life time (τ_r) of the injected electrons in ZnO photoanode can be calculated through the following expression (τ_r) = /2(π f_{max}), where f_{max} is the maximum frequency of the mid-frequency peak. It is clear from the Nyquist plots that the sample showing highest photovoltaic performance has lowest value of f_{max} (highest electron lifetime).[56]Relative electron lifetimes can also be estimated from open circuit voltage decay (OCVD) measurements.[57] Figure S4 shows the OCVD profiles of the devices annealed at various temperatures. As compared to the other samples, the photoanode annealed at 250 °C shows the slowest decay in Voc after light cut-off. This means that the charge recombination process is slowest in this photoanode as compared to others. In other words, the photoanode treated at 250 °C has the highest electron lifetime as compared to others. This results correlate well with the J-V and impedance measurements data.

Figure 6d shows the IPCE spectra of the devices. An IPCE spectrum reflects the light response of the photovoltaic devices, which is directly related to J_{sc}. The device based on the photoanode thermally treated at 250 °C exhibits highest quantum efficiency over the whole spectral range from 400 to 800 nm than that of the other thermally treated ZnO photoanodes. The maximum IPCE of the photoanode was 41.94% at 535 nm whereas other electrodes demonstrate relatively lower- i.e. 8.95%, 29.28%, 23.81% and 24.72% for the as-synthesized 150 °C, 350 °C and 450 °C annealed samoles, respectively. A reason for little increase in IPCE value (also the Jsc) for the 350 °C treated ZnO photoanode is unclear. Considerable increase in IPCE value can be mainly attributed to the good interconnectivity among nanoplates and the adhesion strength. The increase in IPCE is in good agreement with the enhanced value of $J_{sc.}$.

Conclusions

In summary, we have demonstrated an extremely simple but very effective solid-state synthesis method for the fabrication of various metal oxide nanostructures. This method is easily scalable and can be employed for large scale production of crystalline metal oxide powders. As an example for potential application of these metal oxides, we demonstrated the application of ZnO nanoplates as a photoanode in DSSCs. Photoanodes composed of small nanoplates were spongy in nature, ensuring better connections among the nanostructures for the electron transport in the ZnO photoanode, and for the diffusion of redox couples in the electrolyte. We systematically studied the mechanism and the effect of annealing temperature on DSSCs. The device with the low-temperature treated ZnO photoanode obtained using the solid-state reaction has demonstrated a power conversion efficiency of 5%, which is certainly non-ignorable.

Acknowledgements

This research was supported by the KIST Institutional Program (2E23964) and also by Basic Science Research Program through the National Research Foundation of Korea (NRF) funded by the Ministry of Education (2013009768). One of the authors (N.K. Shrestha) is supported by The Korean Federation of Science and Technology Societies under Brain Pool program.

Notes and references

[a]*Department of Chemistry, Hanyang University, Sungdong-Ku, Haengdang-dong 17, Seoul, Republic of Korea 133-791*

[b]*Center for Nanomaterials and Energy Devices, School of Physical Sciences, Swami Ramanand Teerth Marathwada University, Dnyanteerth, Vishnupuri, Nanded 4316006, India*
[c]*Energy Storage Research Centre, Korea Institute of Science and Technology,Hwarangno 14-gil 5, Seongbuk-gu, 136791 Seoul, Republic of Korea*
**Corresponding authors address: Tel.: +822-22925212. FAX: +822-2299-0762.*
E-mail: shhan@hanyang.ac.kr (Prof. S.H. Han)

† Electronic Supplementary Information (ESI) available: [S1: energy-dispersive X-ray spectroscopy spectra and data. S2: (a) N_2 adsorption-desorption isotherms of the photoanode thermally treated at various temperatures, (b) corresponding Barrett–Joyner–Halenda pore-size distribution determined from the N_2 adsorption branch isotherm. S3: Bode phase plots of ZnO nanoplates photoanode thermally treated at various temperatures. S4: electron life time in ZnO photoanode treated at various temperatures]. See DOI: 10.1039/b000000x/

1. B. O'Regan and M. Gra¨tzel , *Nature*, 1991, **353**, 737-740.

2. J. Lee M. C. Orilall, S. C. Warren, M. Kamperman, F. J. DiSalvo and U. Wiesner, *Nat. Mater.*, 2008 , **7** , 222-228.

3. H. J. Bolink, E.Coronado, J. Orozco and M. Sessolo, *Adv. Mater*., 2009, **21**, 79-82.

4. A. V. Emeline, G. V. Kataeva, A. V. Panasuk, V. K. Ryabchuk and N. V. Sheremetyeva, N. Serpone, *J. Phys. Chem. B.*, 2005, **109**, 5175-5185.

5. M. Kroger, S. Hamwi, J. Meyer, T. Riedl, W. Kowalsky and A. Kahn, *Org.Electron*., 2009, **10**, 932-938.

6. M. Gutowski, J. E. Jaffe, C. L. Liu, M. Stoker, R. I. Hegde, R. S. Rai and P. J. Tobin, *Appl. Phys. Lett.*, 2002, **80**, 1897-1899.

7. G. M. Rignanese, *J. Phys.: Condens. Matter*, 2005, **17**, R357-R359.

8. J. Robertson , *Rep. Prog. Phys.*, 2006, **69**, 327-396.

9. K. Chen , A. T. Bell and E. Iglesia1, *J. Catal.*, 2002, **209**, 35-42.

10. V. V. Sysoev, B. K. Button, K. Wepsiec, S. Dmitriev and A. Kolmakov, *Nano Lett.*, 2006, **6**, 1584-1588.

11. A. Dimoulas, M. Houssa, A. Ritenour, J. Fompeyrine, W. Tsai and J. W. Seo, ECS Trans., 2006, **3**, 371-384.

12. M. J. Lee, S. Han, S. H. Jeon, B. H. Park, B. S. Kang, S. E. Ahn, K. H. Kim, C. B. Lee, C. J. Kim, I.-K. Yoo, D. H. Seo, X.-S. Li, J.-B. Park and J.-H. Lee, Y. Park, *Nano Lett.*, 2009, **9**, 1476-1481.

13. J. I. Sohn, Y.-I. Jung, S.-H. Baek, S. Cha , J. E. Jang, C.-H. Cho, J. H. Kim, J. M. Kim and I.-K. Park, *Nanoscale*, 2014, **21**, 2046–2051

14. C.P. Dietrich, M. Lange, M. Stolzel and M. Grundmann, *Appl. Phys. Lett.*, 2012, **100**, 031110-4.

15. D. R. Rosseinsky, R. J. Mortimer, *Adv. Mater.*, 2001, **13**, 783- 793 .

16. C. G. Granqvist, *Sol. Energy Mater. Sol. Cells*, 2008, **92**, 203-208.

17. K. Takada, H. Sakurai, E. Takayama-Muromachi, F. Izumi, R. A. Dilanian and T. Sasaki, *Nature*, 2003, **422**, 53-55.

18. R. S. Devan, R. A. Patil, J.H. Lin and Y. Ron Ma, *Adv. Funct. Mater*., 2012, **22**, 3326-3370.

19. S.Muduli, O. Game, V. Dhas, A. Yengantiwar and S. B. Ogale, *Energy Environ. Sci.*, 2011, **4**, 2835-2839.

20. D. V. Shinde, D.Yeon Lee, S. A. Patil, I. Lim, S. S. Bhande, W. Lee, M. M.Sung, R. S. Mane, N. K. Shrestha and S. H. Han, *RSC Adv.*, 2013, **3**, 9431-9435.

21. K. Tehare, M. K. Zate, S. S. Bhande, S. A. Patil, S. L. Gaikawad, S. J. Yoon, R. S. Mane, S. H. Lee and S. H. Han, *J. Mater. Chem. A*, 2014, **2**, 478-483.

22. S. A. Patil, P.Y. Kalode, R. S. Mane, D. V. Shinde, A. Doyoung, C. Keumnam, M. M. Sung, S. B. Ambade and S. H. Han, *Dalton Trans.*, 2014, **43**, 5256-5259.

23. S. B. Ambade, R. B. Ambade, R. S. Mane, G. W. Lee, S. F. Shaikh, S. A. Patil, O. S. Joo, S. H. Han and S. H. Lee, Chem. Commun., 2013, **49**, 2921–2923..

24. S. A. Patil, D. V. Shinde, E. Kim, J. K. Lee, R. S. Mane and S. H. Han, *RSC Adv.*, 2012, **2**, 11808-11812.

25. S. A. Patil, D. V. Shinde, S. S. Bhande, V. V. Jadhav, T.N. Huan, R. S. Mane and S.H. Han, *Dalton Trans.*, 2013, **42**, 13065-13070.

26. H. W. Kang, J. Leem, S. Y. Yoon and H. J. Sung, *Nanoscale*, 2014, **6**, 2840-2846.

27. J. Liu, S. Zou, S. Li, X. Liao, Y. Hong, L. Xiao and J. Fan, *J. Mater. Chem. A*, 2013, **1**, 4038-4047.

28. H. Wang, D. Ma, X. Huang, Y. Huang and X. Zhang, *Scientific reports*, **2**,701-708.

29. L. Han, D. Wang, J. Cui, L. Chen, T. Jiang and Y. Lin, *J. Mater. Chem.*, 2012, **22**, 12915-12920.

30. S. L. Bai, J. W. Hu, D. Q. Li, R. X. Luo, A. F. Chen and C. C. Liu, *J. Mater. Chem.*, 2011, **21**, 12288–12294.

31. X. Sun, H. Zhang, J. Xu, Q. Zhao, R. Wang and D. Yu, *Solid State Commun*., 2004, **129**, 803-807.

32. M. Wang, C. H. Ye, Y. Zhang, G. M. Hua, H. X. Wang, M. G. Kong and L. D. Zhang, J. *Cryst.* Growth, 2006, **291**, 334-339.

33. D. Li , Y. N. Xia, *Nano Lett*., 2003, **3**, 555-560.

34. T. Thurn-Albrecht, J. Schotter, C. A. Kastle, N. Emley,T. Shibauchi, L. Krusin-Elbaum, K. Guarini, C.T. Black, M. T. Tuominen and T. P. Russell, *Science*, 2000, **290**, 2126-2129.

35. P. D. Cozzoli, A. Kornowski and H. Weller, *J. Am. Chem. Soc*., 2003, **125**, 14539-14548.

36. H. M. Xiong, D.G. Shchukin, H. Möhwald, Y. Xu, Y. Y. Xia, *Angew. Chem.*, 2009 , **121**, 2765–2769.

37. J. Liu, L. Xu, B Wei, W. Lv, H. Gao and X. Zhang, CrystEngComm**,** 2011,**13**,1283-1286.

38. H.-Y. Jiang, Kun Cheng and Jun Lin. *Phys. Chem. Chem. Phys.*, 2012, **14**, 12114-12121.

39. S. S. Bhande, R. S. mane, A. V. Ghule and S. H. Han, *Scripta Materialia*, 2012, **65**, 1081-1084.

40. K. Sakaushi, Y. Oaki, H. Uchiyama, E. Hosono, H. Zhou and H Imai, *Nanoscale*, 2010, **2**, 2424-2430.

41. Q. F. Zhang, C. S. Dandeneau, X. Y. Zhou, G. Z. Cao, *Adv. Mater*., 2009 , **21** , 4087-4108.

42. E. Guillén, L. M. Peter, J. A. Anta, *J. Phys. Chem. C* , 2011, **115**, 22622–22632.

43. E. Guillén, E.Azaceta, L. M. Peter, A. Zukal, R. Tena-Zaera and J. A. Anta , J. *Energy Environ Sci.*, 2011, **4**, 3400– 3407.

44. X. Yin, B. Wang, M. He and T. He, *Nano Res*., 2012, **5,** 1-10.

45. A. Kargar, Y. Jing, S. J. Kim, C. T. Riley, X. Q. Pan and D. L. Wang *ACS Nano*, 2013, 7, 11112-11120.

46. F. Jin, X. Yuan, W. W. Ge, J. -M. Hongand and X.-Q. Xin, *Nanotechnology*, 2003, **14**, 667-669.

47. E. Guillén, C. Fernández-Lorenzo, R. Alcántara, J. Martín-Calleja and J. Anta, *Sol. Energy Mater.Sol. Cells*, 2009, **93**, 1846–1852.

48. R. -O. Moussodia, L. Balan, C. Merlin, C. Mustin and R. Schneider, *J. Mater. Chem.*, 2010, **20**,1147-1155.

49. J. Zhang, M. He, N. Fu ' J. Li and X.Yin, *Nanoscale*, 2014, **6**, 4211-4216.

50. M. Ahmad, C. Pan and J. Zhu *J. Mater. Chem.*, 2010, **20**, 7169-7174.

51. F. F. Santiago, J. Bisquert, G. G. Belmonte, G. Boschloo and A. Hagfeldt, *Sol. Cells*,2005, **87,** 117-131.

52. Q. Zhang, T. P. Chou, B. Russo, S. A. Jenekhe and G. Cao, *Angew. Chem., Int. Ed.*, 2008, **47**, 2402-2406 .

53. G. Z. Xing, B. Yao, C. X. Cong, T. Yang, Y. P. Xie, B. H. Li and D. Z. Shen, *J. Alloys Compd*., 2008, **457** ,36-41.

54. C. Y. Liu, Y. H. Lai, H. W. Chen, J. G. Chen, C. W. Kuang, R. Vittal and K. C. Ho, *Energy Environ, Sci.*, 2011, **4**, 3448-3455.

55. J. van de Lagemaat, N. G. Park and A. J. Frank, *J. Phys. Chem. B,* 2000, **104**, 2044–2052.

56. D. Zhao , T. Peng, L. Lu, P. Cai, P. Jiang and Z. Bian *J. Phys. Chem. C*, 2008, **112**, 8486-8494.

57. A. Zaban, M. Greenshtein and J. Bisquert, *ChemPhysChem*, 2003, **4**, 859-864.

Cite this: DOI: 10.1039/c0xx00000x

www.rsc.org/xxxxxx

ARTICLE TYPE

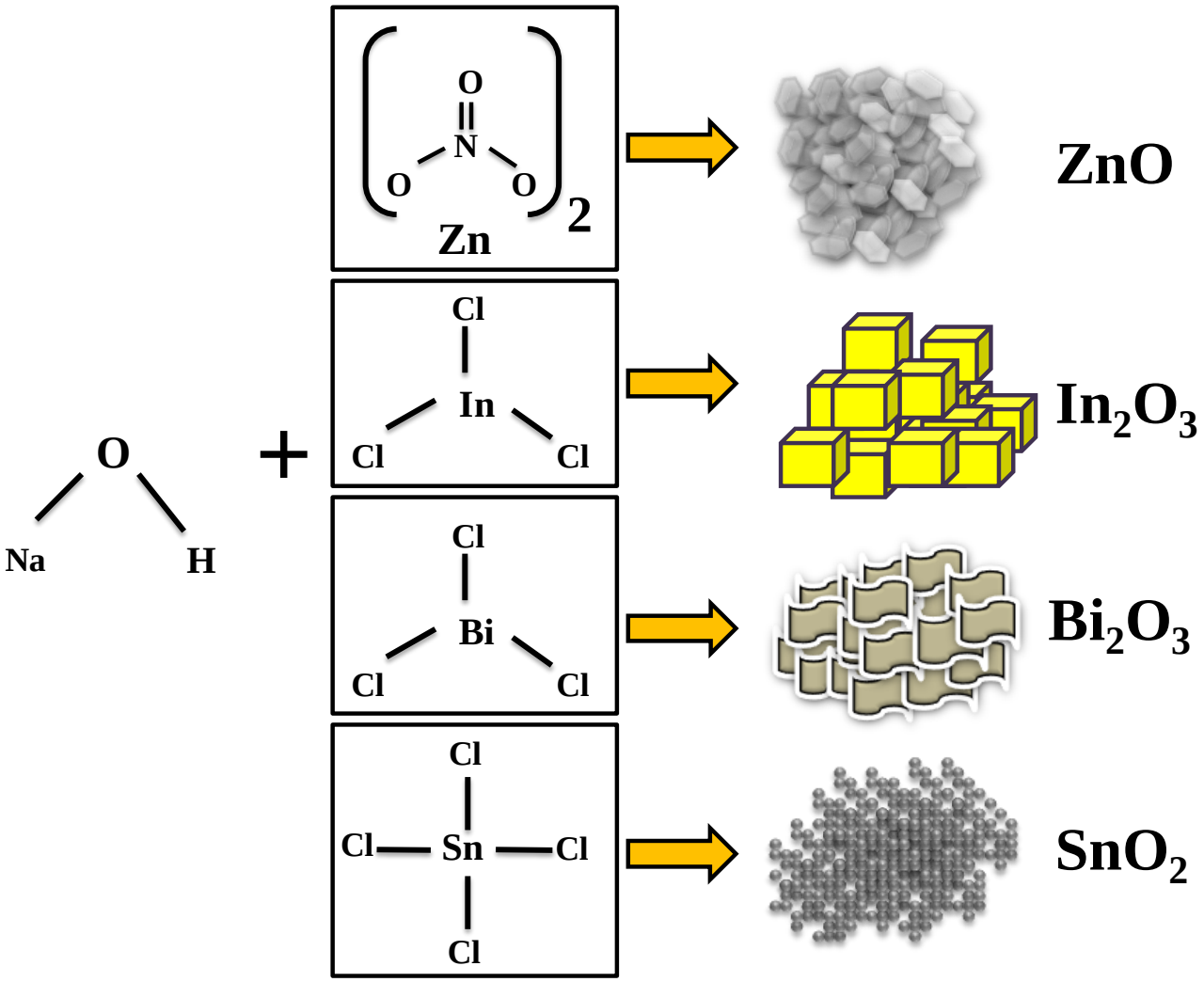

Scheme 1. A schematic representation of the reaction between various metal ion precursors and sodium hydroxide in solid state, and thereby producing the corresponding metal oxides.

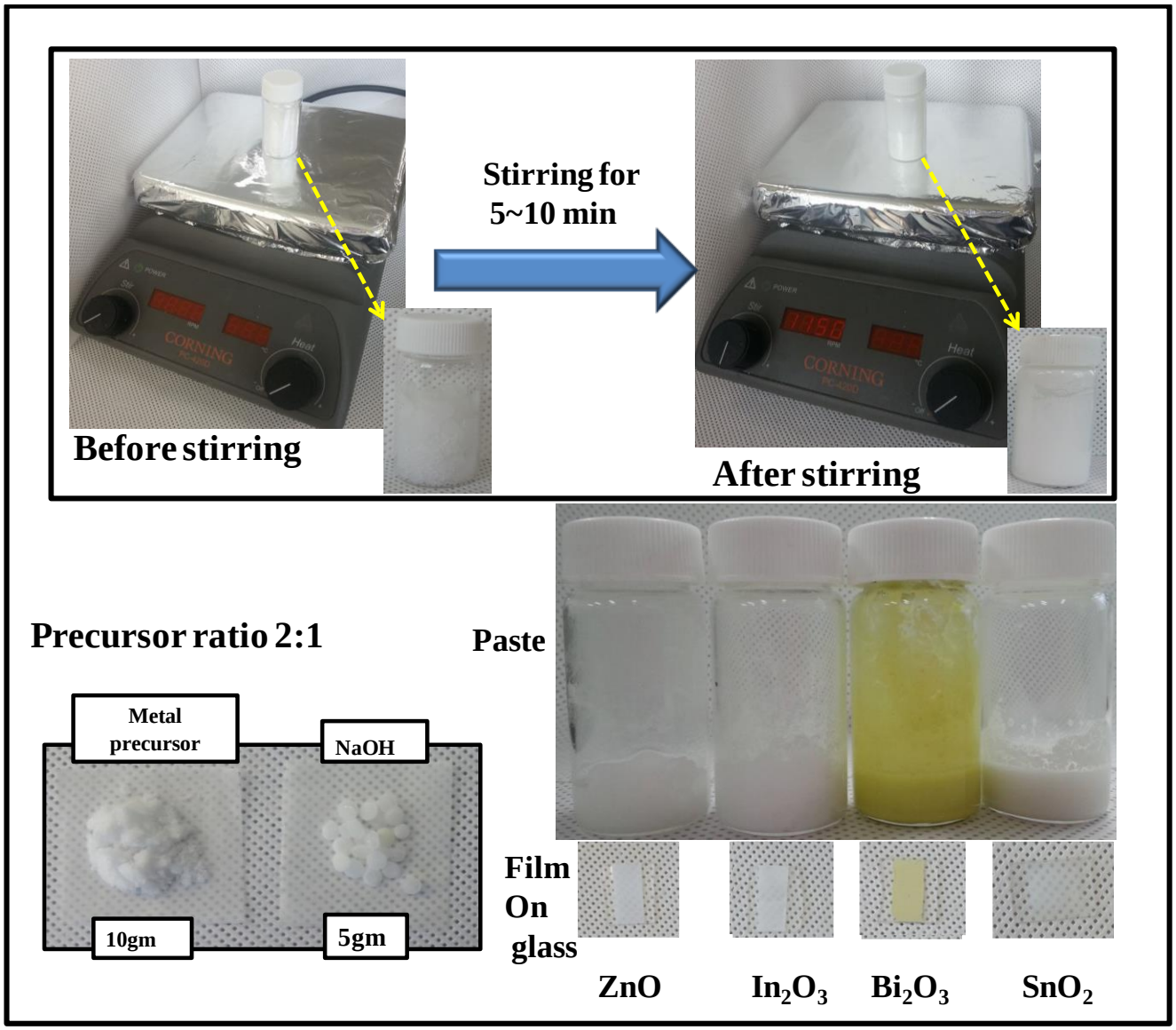

Figure 1: Experimental setup for synthesis of various functional metal oxides (MOs). The bottom images shows MO slurry formed after 5~10 min of reaction, which can be directly applied on various substrates by doctor blade method.

Cite this: DOI: 10.1039/c0xx00000x

www.rsc.org/xxxxxx

ARTICLE TYPE

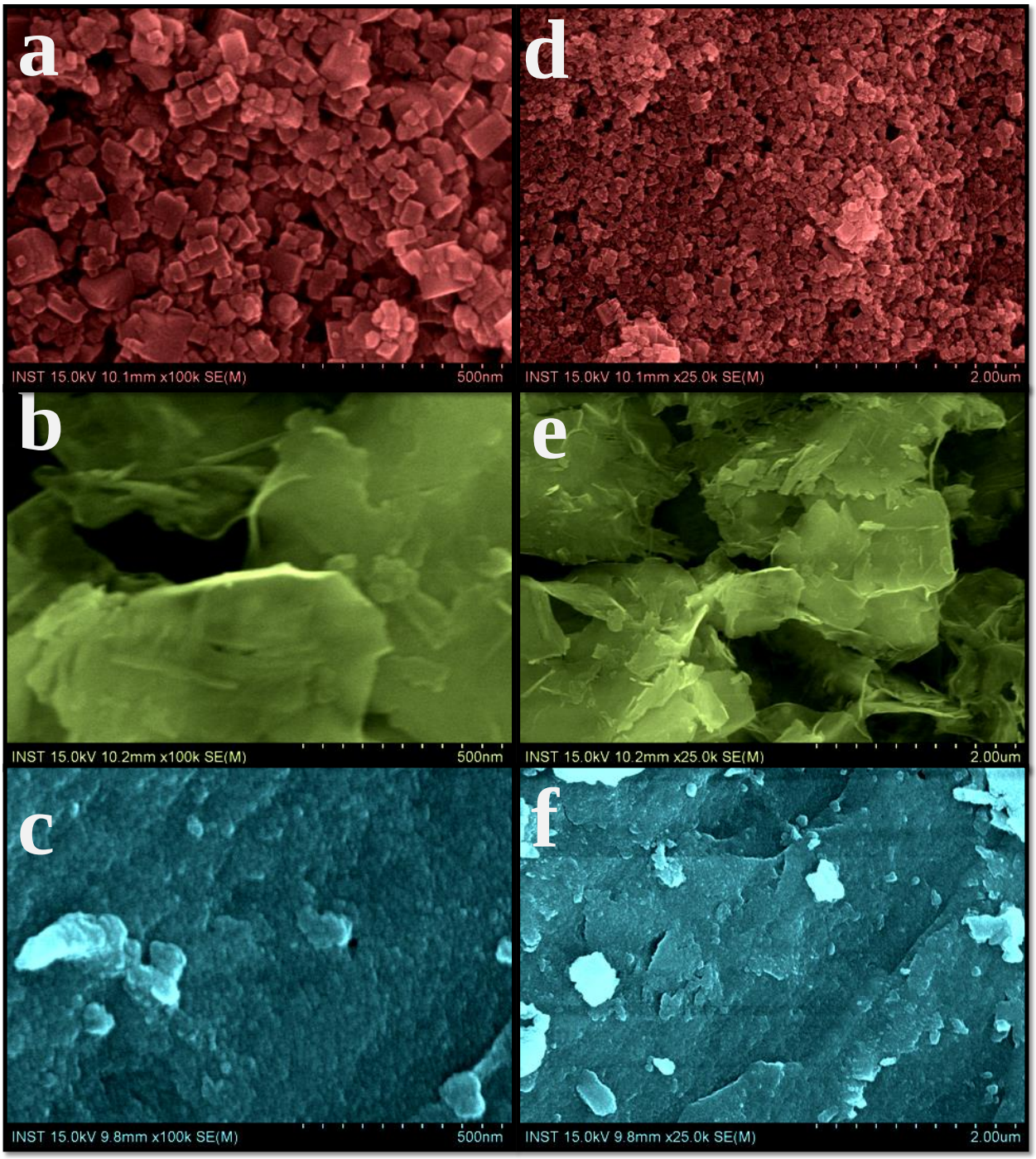

Figure 2. Scanning electron microscope images (false colour) of the MO nanostructures obtained by solid state synthesis. (a) In_2O_3, (b) Bi_2O_3, and (c) SnO_2 nanostructures on FTO substrates. (d), (e) and (f) are low magnification SEM images of the respective MO nanostructures.

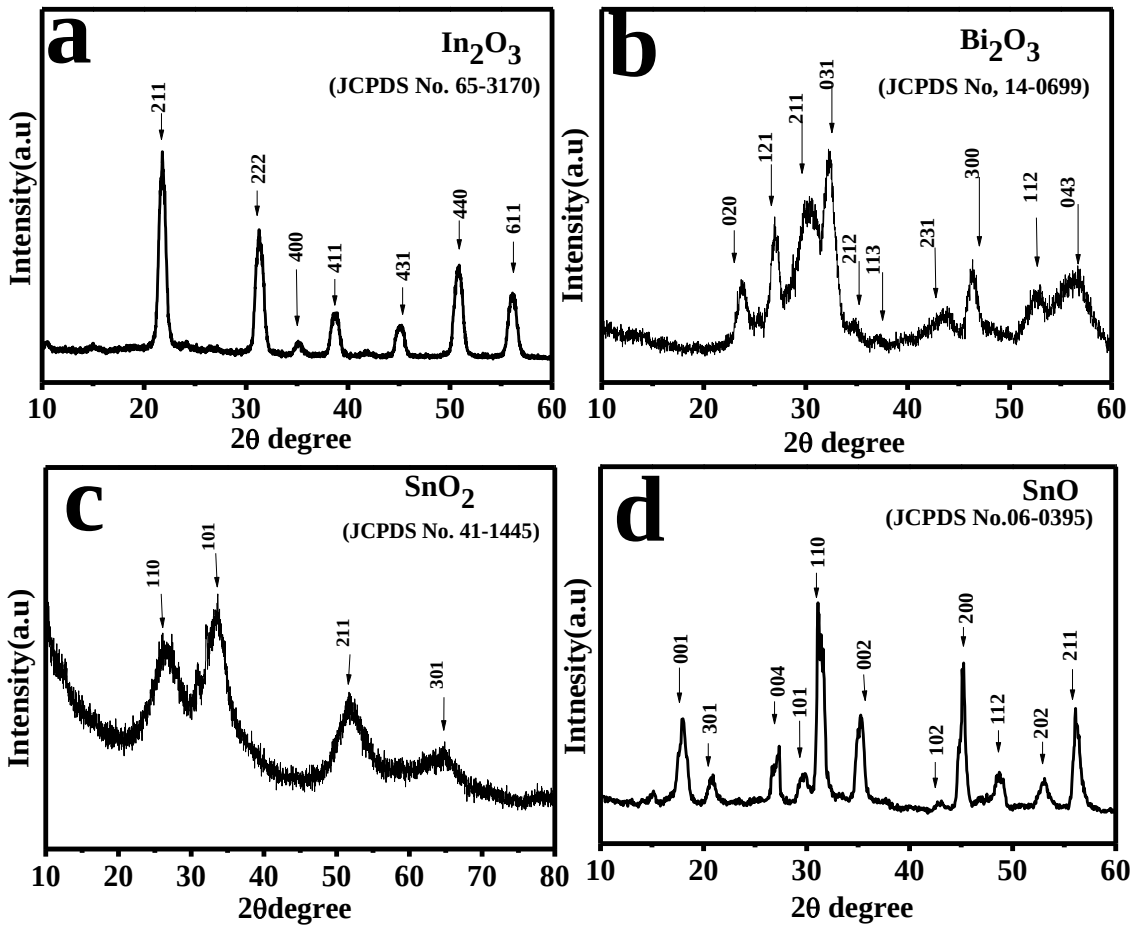

Figure 3. XRD pattern of the MO nanostructures obtained by solid state synthesis. (a) In_2O_3, (b) Bi_2O_3, (c) SnO_2, and (d) SnO (obtained using $SnCl_2$ precursor) nanostructures.

Cite this: DOI: 10.1039/c0xx00000x

www.rsc.org/xxxxxx

ARTICLE TYPE

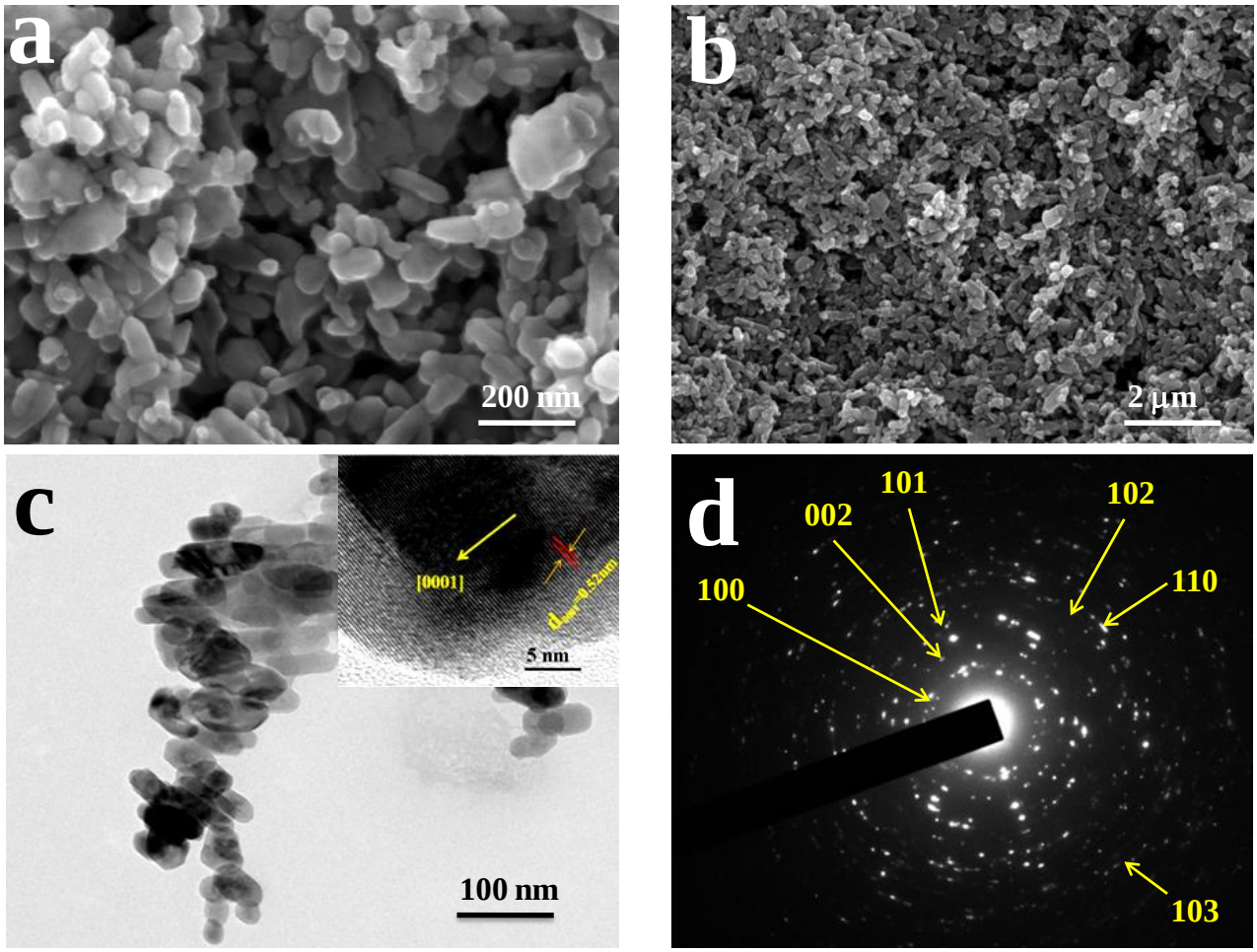

Figure 4. (a) SEM image of ZnO nanoplates, (b) the same film at low magnification showing porous film consisting of nanoplate nanostructures, (c) low resolution TEM (Inset: high-resolution TEM) image of the ZnO nanoplates, and (d) corresponding selected area electron diffraction pattern (SAED).

Cite this: DOI: 10.1039/c0xx00000x

www.rsc.org/xxxxxx

ARTICLE TYPE

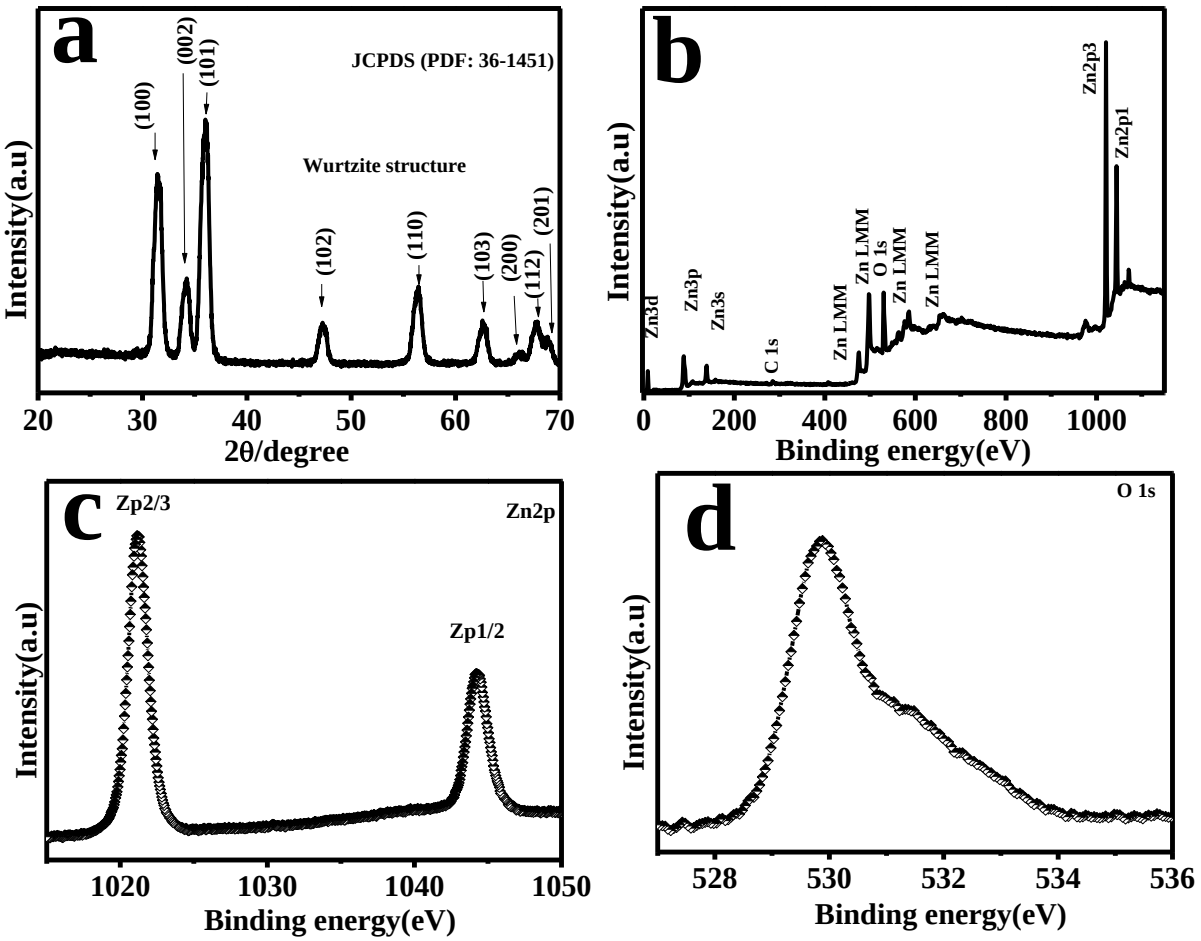

Figure 5. (a) XRD pattern, (b) XPS survey spectrum, (c) Zn 2p, and (d) O1s core levels XPS spectra of ZnO nanoplates.

Cite this: DOI: 10.1039/c0xx00000x

www.rsc.org/xxxxxx

ARTICLE TYPE

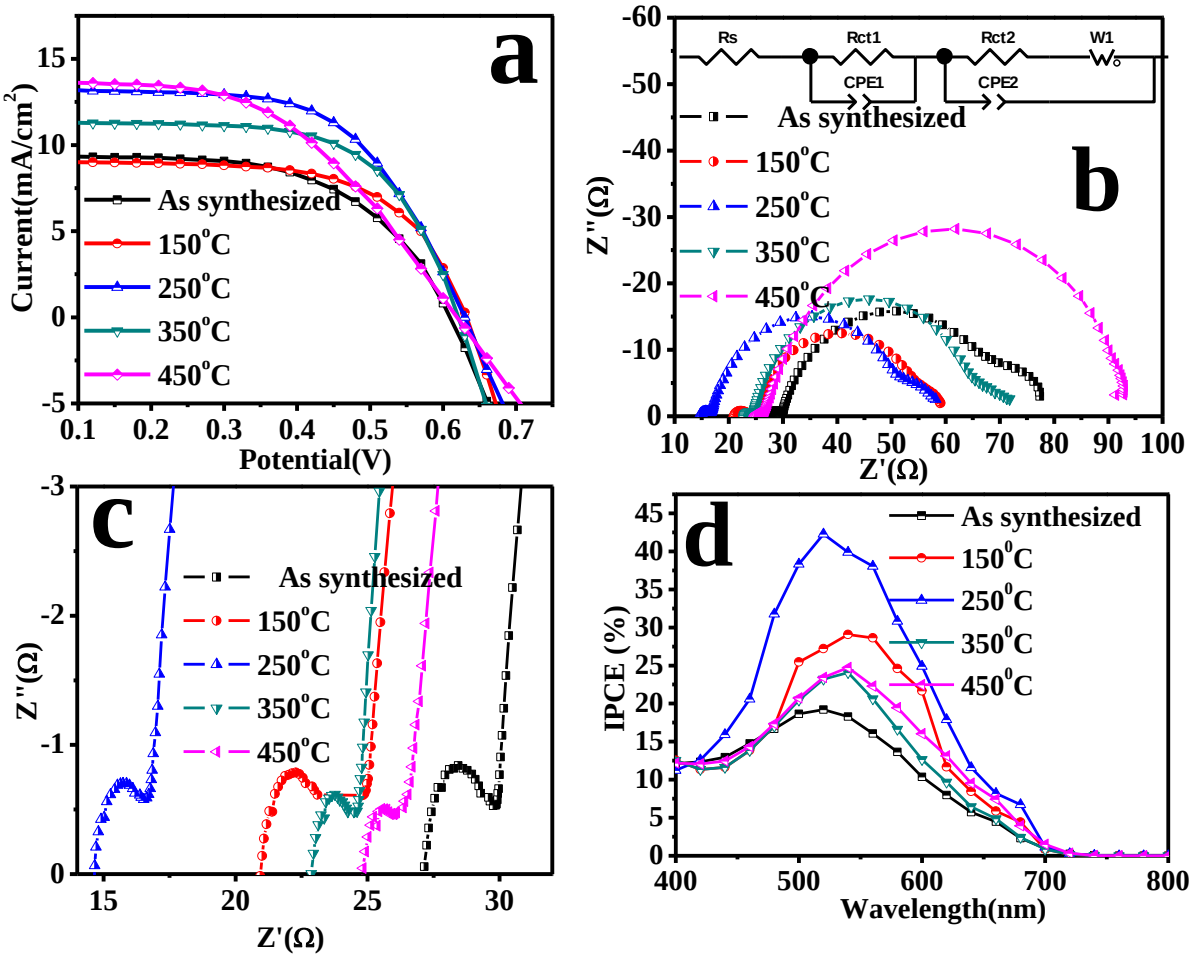

Figure 6. (a) J-V curves of DSSCs consisting of a ZnO photoanode. (b) Nyquist plots of DSSCs employing ZnO photoanodes annealed at various temperatures. (c) Nyquist plots zoomed at high frequency region (inset shows the equivalent circuit diagram used to fit the experimentally obtained impedance data). (d) IPCE spectra of various ZnO photoanodes.

Cite this: DOI: 10.1039/c0xx00000x

www.rsc.org/xxxxxx

ARTICLE TYPE

Photoanode Annealing Temp.	Voc	Jsc (mA/cm^2)	FF	η%	Adsorbed dye × 10^{-7} $molcm^{-2}$	Rs	Rct_1	Rct_2
As -Synthesized	0.60	9.40	0.58	3.3	2.33	33.50	3.29	62.5
150 °C	0.63	9.09	0.63	3.6	2.72	20.99	3.71	31.62
250 °C	0.63	13.31	0.60	5.0	2.91	14.30	2.94	37.28
350 °C	0.62	11.41	0.64	4.5	2.86	21.42	3.01	45.28
450 °C	0.61	13.74	0.54	4.1	2.84	22.72	2.87	42.09

Table 1. Detailed photovoltaic and imedance paramters summarized from the *J-V* curves and Nyquist plots from Figure 6.

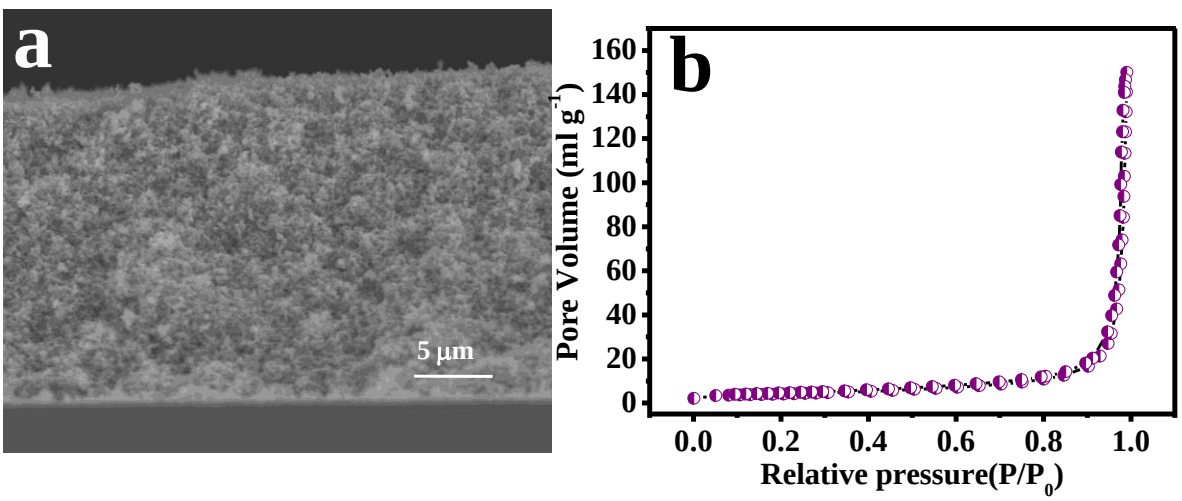

Figure 7. (a) Cross-section SEM image of a ZnO photoanode. (b) N_2 adsorption-desorption isotherms of the photoanode thermally treated at 250°C.